1   **SARS-CoV-2 spike D614G variant exhibits highly efficient replication and transmission**

2   **in hamsters**

3   Bobo Wing-Yee Mok[1], Conor J. Cremin[1], Siu-Ying Lau[1], Shaofeng Deng[1], Pin Chen[1], Anna

4   Jinxia Zhang[1], Andrew Chak-Yiu Lee[1], Honglian Liu[1], Siwen Liu[1], Timothy Ting-Leung Ng[2],

5   Hiu-Yin Lao[2], Eddie Lam-Kwong Lee[2], Kenneth Siu-Sing Leung[1], Pui Wang[1], Kelvin Kai-

6   Wang To[1], Jasper Fuk-Woo Chan[1], Kwok-Hung Chan[1], Kwok-Yung Yuen[1], Gilman Kit-Hang

7   Siu[2] and Honglin Chen[1*]

8

9

10   [1]Department of Microbiology and State Key Laboratory for Emerging Infectious Diseases, Li

11   Ka Shing Faculty of Medicine, The University of Hong Kong, Hong Kong SAR, China.

12   [2]Department of Health Technology and Informatics, Faculty of Health and Social Sciences,

13   The Hong Kong Polytechnic University, Hong Kong SAR, China

14

15   ***Correspondence:** hlchen@hku.hk

16

17 **Summary**

18 SARS-CoV-2 causes disease varying in severity from asymptomatic infections to severe

19 respiratory distress and death in humans. The viral factors which determine transmissibility

20 and pathogenicity are not yet clearly characterized. We used the hamster infection model to

21 compare the replication ability and pathogenicity of five SARS-CoV-2 strains isolated from

22 early cases originating in Wuhan, China, in February, and infected individuals returning from

23 Europe and elsewhere in March 2020. The HK-13 and HK-95 isolates showed distinct

24 pathogenicity in hamsters, with higher virus titers and more severe pathological changes in the

25 lungs observed compared to other isolates. HK-95 contains a D614G substitution in the spike

26 protein and demonstrated higher viral gene expression and transmission efficiency in hamsters.

27 Intra-host diversity analysis revealed that further quasi species were generated during hamster

28 infections, indicating that strain-specific adaptive mutants with advantages in replication and

29 transmission will continue to arise and dominate subsequent waves of SARS-CoV-2

30 dissemination.

31

32 **Keywords:** Coronavirus, SARS-CoV-2, COVID-19, Spike, D614G, transmission, hamster

33

Introduction

A newly emerged β-coronavirus, SARS-CoV-2, which causes COVID-19 disease in humans, attained cross species transmission through a process yet to be defined in detail (Andersen et al., 2020; Wu et al., 2020; Zhou et al., 2020a). Human cases were first identified in Wuhan, China, in December 2019 and SARS-CoV-2 subsequently disseminated worldwide leading to the announcement of a global pandemic by the World Health Organization on March 11, 2020 (Mahase, 2020). More than 20 million laboratory-confirmed cases and over 700,000 deaths have been recorded globally to date (https://coronavirus.jhu.edu/map.html) (Dong et al., 2020) . In contrast to SARS-CoV and MERS-CoV, a significant number of SARS-CoV-2 infections are asymptomatic. However, in areas high virus activity a substantial portion of infections lead to severe disease or death (Chen et al., 2020b). While aging and certain underlying medical conditions may predispose individuals to increased severity of COVID-19 disease (Zhang et al., 2020c), it is not clear if viral factors may also contribute to the variable pathogenicity of SARS-CoV-2 in humans (Becerra-Flores and Cardozo, 2020). It is expected that SARS-CoV-2 will continue to be transmitted among humans globally, leading to the emergence of more phenotypic variants. It is therefore important to define the viral factors associated with transmissibility and pathogenicity of SARS-CoV-2. Analysis of a mutant virus with a deletion at the spike protein S1/S2 junction showed that the PRRA polybasic cleavage site is associated with heightened pathogenicity in the model (Lau et al., 2020b). SARS-CoV-2 is of zoonotic origin and is currently in the process of becoming more adapted to humans as it circulates and acquires adaptative mutations. Different variants have already been identified among clinical specimens and in cultured isolates (Gong et al., 2020; Su et al., 2020). Some deletion or mutation variants may not be recognized by general sequencing protocols, for which the readout only shows the dominant population in clinical specimens or cell culture samples, but can be detected by more sensitive methods (Wong et al., 2020).

SARS-CoV-2 was first identified in China in December 2019 (Wu et al., 2020; Zhou et al., 2020a). A response adopting aggressive control measures, including the lock down of a city of 10 million people (Wuhan) and the wider Hubei Province (population: 56 million) in January 2020, significantly limited the further dissemination of the virus within China (Ji et al., 2020; Lau et al., 2020a). SARS-CoV-2 has been efficiently transmitting among humans since it was first recognized, according to studies from the early outbreak (Chan et al., 2020a; Liu et al., 2020). Subsequent transmission of SARS-CoV-2 in Europe, the US and other countries has resulted in more widespread human infections since March 2020. As more humans are exposed to the SARS-CoV-2 virus, it is expected that more host adapted phenotypic variants of the virus

68   will emerge. It is important to determine whether some emerging variants may have the

69   potential to go on to become the dominant strain in the coming waves of circulation. Indeed, a

70   strain bearing a D614G mutation in the spike protein, first observed in January 2020 among

71   isolates from China and Europe, has since become the dominant population in the recent

72   transmissions occurring in Europe and the US (Korber et al., 2020). Studies using pseudo-

73   viruses containing spike genes derived from natural isolates have shown that variants harboring

74   D614G infect cells more effectively (Daniloski et al., 2020; Zhang et al., 2020b). Although

75   D614G is in the spike protein, the D614G variant is still susceptible to neutralization by

76   antibodies raised against strains lacking this mutation (Korber et al., 2020). To further

77   understand the properties of the D614G variant, we analyzed pathogenicity, virus replication

78   efficiency and the global transcriptome of the host response in the airways of SARS-CoV-2

79   D614G variant infected hamsters. Although it is not clear if the D614G variant causes more

80   severe disease in humans, our data showed that SARS-CoV-2 containing D614G replicates

81   more efficiently and causes more severe pathological changes in the lung tissues of infected

82   animals when compared to isolates lacking this mutation.

83

4

84 **Results**

85 **SARS-CoV-2 genomic variants exhibit variable pathogenicity in hamsters**

86 Five isolates were selected to study variability in the pathogenicity of SARS-CoV-2

87 strains and the host response to such variants in a hamster infection model. These strains

88 represent isolates from the early outbreak in China (HK-8, HK-13 and HK-15) and subsequent

89 outbreaks in Europe and elsewhere (HK-92 and HK-95) (Table S1). Phylogenetic analysis

90 revealed that these strains belonged to distinctive GISAID phylogenetic clades (**Figure S1**).

91 The sequences of these five isolates were compared with that of the index isolate (Wuhan-Hu-

92 1), characterized during the early outbreak in Wuhan city, China (Wu et al., 2020; Zhou et al.,

93 2020a), revealing a range of variations in the untranslated region and *Orf1a*, *Orf1b*, *Orf3*, *Orf8*,

94 *N* and *S* genes among strains (**Table 1**). HK-95 is an isolate characterized from a traveler

95 returning to Hong Kong from Egypt and carries a D614G substitution in the spike gene (**Figure**

96 **S1**). Hamsters are a highly susceptible model for studying SARS-CoV-2 infection, with disease

97 in hamsters closely simulating COVID-19 disease in humans (Chan et al., 2020b). Infection

98 progresses rapidly in hamsters, but infected animals then recover after about one-week of

99 infection. We infected hamsters with these five strains of SARS-CoV-2 and monitored disease

100 presentation for 5 days. All five isolates caused significant body weight loss compared to the

101 control group (**Figure 1A**). In SARS-CoV-2-infected hamsters, three major histopathological

102 changes were observed in lungs: various degrees of bronchial or bronchiolar inflammation

103 (bronchiolitis), lung parenchymal inflammatory damage (alveolitis) and pulmonary blood

104 vessel inflammation (vasculitis). These pathological changes were most severe at day 5 after

105 virus inoculation. The HK-13 and HK-95 isolates caused more extensive bronchiolar cell death,

106 diffuse alveolar space exudation and infiltration and lung consolidation, compared to HK-8

107 (**Figure 1B**). In our previous report, at day 4 post-infection (pi) with HK-001a virus, alveoli

108 had already started to show focal areas of cell proliferation indicating resolution of

109 inflammation (Chan et al., 2020b; Lau et al., 2020b). However, such indications of resolution

110 were not seen in HK-95- or HK-13-infected hamsters, even at day 5 post-infection, indicating

111 that the acute lung inflammation caused by both of these strains may last longer than that

112 triggered by infection with other SARS-CoV-2 strains.

113 **Differences in replication rates of SARS-CoV-2 isolates in infected hamsters**

114 Examination of virus titers in lung tissues and nasal washes at day 5 post-infection

115 showed that HK-13 and HK-95 replicate to significantly higher levels than the other three

116 isolates (**Figure 2A and S2**). We then analyzed viral gene expression in the lung tissues of

117 hamsters infected with different isolates using RNA-seq analysis. Consistent with the virus

118   titers, viral gene expression also showed a similar distribution between isolates when

119   comparing the average expression of all viral genes per isolate (black line) to viral titer profiles

120   (**Figure 2B**). Interestingly, the expression distribution between each of the viral genes for each

121   isolate is very similar across all isolates, with differences in overall expression being due to a

122   proportional change in expression across all genes. This indicates that the observed differences

123   in viral gene expression can be attributed to isolates maintaining different rates of replication.

124   These differences in replication suggest that some viral isolates may be more constrained by

125   host-specific factors and as such are unable to achieve an optimal rate of replication, as is seen

126   for HK-8. This also implies that individual isolates interact differently with their hosts during

127   the infection process. To assess if constraints to viral replication are reflected in the severity of

128   the host response induced by SARS-CoV-2 infection, we performed an initial characterization

129   of the hamster host response to infection.

130   **Differential expression of SARS-CoV-2 genes and host response in hamsters**

131   To further understand the global host response elicited by difference isolates, we

132   grouped the samples in a principal component analysis (PCA) (Figure 2C). In this PCA space,

133   we observed transcriptional perturbations along the two principal components, both account

134   for more than 25% of sample variation (Figure 2C). This analysis suggested unique expression

135   signatures in hamster host responses to infection with different SARS-CoV-2 isolates. In

136   addition, volcano plots show that viral isolates HK-13 and HK-95, which demonstrate higher

137   rates of replication than isolate HK-8, incited significant upregulation of host gene expression

138   compared to HK-8 (**Figure 3**). Unsurprisingly, the host responses provoked by HK-8 and HK-

139   15 were similar, as these isolates share a similar replication rate. These profiles suggest that

140   higher rates of SARS-CoV-2 replication are a significant driving factor in triggering host

141   responses, which may associate with greater disease severity in humans (Blanco-Melo et al.,

142   2020; Zhou et al., 2020b). However, the differential expression profile generated by comparing

143   HK-8 to HK-92 is similar to that of HK-8 vs HK-95. Since HK-92 has a considerably lower

144   replication efficiency than HK-95 in hamsters (**Figure 2**), this suggests that factors independent

145   of the replication of HK-92 are also involved in inducing the significant upregulation of host

146   gene expression seen here. This offers an explanation as to the close coordinate positioning of

147   HK-92 to HK-95 in our PCA analysis (**Figure 2C**), and why HK-13 is positioned further away,

148   despite possessing a similar replication rate to HK-95 (**Figure 2A and S2**). Our analysis has

149   made it clear that the upregulation of the host response is heavily dependent on the specific

150   viral SARS-CoV-2 isolate that is causing infection. Although viral replication is a significant

6

151 driver in stimulating the host response in hamsters, SARS-CoV-2 appears to have developed

152 replication-independent strategies to influence responses in infected hosts.

153   Hamsters have proven to be a useful live model for studying the dynamics of viral

154 infection and are now routinely used to assess SARS-CoV-2 pathogenesis (Chan et al., 2020b;

155 Lau et al., 2020b; Zhang et al., 2020a). However, the current annotation that is available to

156 describe gene functionality and perform network analysis in hamsters is limited. Therefore, we

157 opted to use the gene functional annotation of a well-defined animal model within close

158 evolutionary distance of the hamster. Our evolutionary analysis identified mice as being

159 suitably closely related to hamsters (**Figure S3**). Therefore, our gene enrichment analysis of

160 differentially expressed hamster-mouse gene orthologues using mouse Gene Ontology (GO)

161 annotation is anticipated to give a fair representation of the induced host response to SARS-

162 CoV-2, without enrichment of redundant hamster-specific processes. GO enrichment analysis

163 identified many functional groups corresponding to T-cell activation and chromatin remodeling

164 as being the networks most significantly upregulated by SARS-CoV-2 infection, regardless of

165 viral isolate used, when compared to samples from uninfected hamsters (**Figure 4**). Activation

166 of T-cells is indicative of upregulation of the adaptive immune response and the host's attempts

167 to restrict viral pathogenesis. The upregulation of chromatin remodeling pathways indicates

168 significant disruption to DNA architecture and an increase in nuclear repair processes,

169 potentially due to cellular stress caused by the SARS-CoV-2 virus during infection. We also

170 conducted GO enrichment analysis of differentially expressed genes in hamster lungs induced

171 by the various SARS-CoV-2 isolates, this time conducting comparisons to samples from HK-

172 95 hamster infections. Our result indicates that subverted gene networks are subject to strain

173 specific targeting processes by the more pathogenic strains of SARS-CoV-2, but not by HK-8

174 (**Figure S4**). Overall, the main effects of SARS-CoV-2 infection involved activation of the T

175 cell response and disruption of regulatory processes in the nuclear microenvironment of

176 infected cells.

D614G variant demonstrates higher transmissibility in hamsters

178   Surveillance of the evolution of SARS-CoV-2 during circulation in humans has

179 identified various mutations which may relate to the infectivity of virus (Chen et al., 2020a;

180 Korber et al., 2020) The spike D614G variant of SARS-CoV-2 has been the clearly dominant

181 population since March 2020, suggesting that it has enhanced infectivity in humans (Becerra-

182 Flores and Cardozo, 2020; Daniloski et al., 2020; Zhang et al., 2020b). We conducted an

183 experiment using the hamster model to examine if the transmission ability of the HK-95 strain,

184 which carries spike D614G, may be enhanced compared to two other isolates (HK-8 and HK-

7

185   13) which lack the D614G substitution (**Figure S5**). Notably, higher virus titers were found in

186   the lung and nasal turbinate tissues of recipient hamsters co-housed with HK-95-infected

187   hamsters than in those secondarily exposed to HK-8 or HK-13 (**Figure 5A**), which differs from

188   the direct infection experiment, where HK-13 and HK-95 demonstrated similar viral titers in

189   respiratory tissues **(Figure 2A and S2)**. We did not examine if naive hamsters in the HK-95

190   group were infected at an earlier time point than those in other groups due to limited availability

191   of experimental animals. But given the higher viral titers in the lung and nasal turbinate tissues,

192   it is possible that hamsters co-housed with a HK-95-infected hamster were infected earlier than

193   those co-housed with hamsters infected with HK-8 or HK-13, and that this facilitated greater

194   virus replication in recipients. It is unclear how the D614G mutation affects virus replication.

195   The efficiency of spike protein cleavage is known to associate with coronavirus replication

196   (Hoffmann et al., 2020; Jaimes et al., 2020). We found that introduction of the D614G mutation

197   into the Wuhan-Hu-1 prototype sequence enhanced SARS-CoV-2 spike cleavage in cells

198   (**Figure 5B**). Since D614G is not located at either of the cleavage sites in the spike protein of

199   SARS-CoV-2, the molecular basis of this effect remains to be investigated. Taken together,

200   these results confirm that acquisition of D614G promotes SARS-CoV-2 infectivity in a

201   mammalian model of SARS-CoV-2 infection.

202   **Intra-host diversity in infected hamsters**

203   To examine intra-host diversity of the different SARS-CoV-2 strains, nasal washes

204   were collected from infected hamsters at days 3 and 5 post-infection and whole genome

205   sequencing conducted to determine the stability of the viral genome over the course of infection.

206   As inferred by Illumina sequencing data, even minor genome variant populations (i.e. variants

207   with frequency < 0.3) identified in the original inoculating strains **(Table 1)** remained present

208   after 5 days of infection (**Table S2**). Interestingly, some genome variants, which were absent

209   in the original strains, developed during hamster infection. The frequencies of these newly

210   arisen variants were generally higher at 5 dpi than at 3 dpi (**Table S2**). This trend of increase

211   implied that these new variants survive better in hamsters. Of note, there was no mixed

212   population observed in HK-95, either in the original isolate or in animals after infection, which

213   may indicate that the D614G variant has acquired a relatively stable genome constellation for

214   replication in mammals; this stability in both human isolates and hamster infections also further

215   supports the contention that hamsters are a suitable model for human SARS-CoV-2 infection.

216

Discussion

217

218   SARS-CoV-2 continues to transmit globally and since its emergence in December 2019

219   has caused more than 20 million laboratory confirmed infections and over 0.7 million deaths,

220   as of August 26 2020. Social distancing strategies have been adopted to slow down the

221   dissemination of virus, in hope that effective vaccines and therapeutics will be developed and

222   available soon enough to prevent further waves of transmission. More than seven months after

223   transmission in humans was first observed, various genetic variants of SARS-CoV-2 have

224   emerged and been analyzed but no clear evolutionary direction for SARS-CoV-2 is yet

225   apparent (Deng et al., 2020; Fauver et al., 2020; Forster et al., 2020; Sanchez-Pacheco et al.,

226   2020). Since the majority of people remain naive to this virus it is necessary to closely track

227   any potential changes in the pathogenic properties of SARS-CoV-2 variants along the course

228   of transmission. SARS-CoV-2 is of zoonotic origin and is expected to gain more adaptations

229   as it circulates in humans. Attenuated variants with deletions in the spike protein S1/S2 junction

230   and other regions have been detected in virus-infected cell cultures and in patient specimens

231   (Lau et al., 2020b; Wong et al., 2020). One variant containing D614G in the spike protein has

232   become the dominant population in many countries since March 2020 and is reported to infect

233   cells more efficiently *in vitro* (Daniloski et al., 2020; Li et al., 2020; Zhang et al., 2020b). To

234   understand if D614G variant virus may exhibit altered pathogenicity and transmissibility, we

235   compared 5 SARS-CoV-2 isolates obtained from Hong Kong returnees from Wuhan, China,

236   in February and travelers who had visited Europe and other countries after March 2020, using

237   the hamster infection model. We found that the D614G bearing strain, HK-95, replicates more

238   efficiently in the airways of infected hamsters in the lungs than strains lacking D614G (**Figure**

239   **2 and S2**). A contact transmission experiment showed that naive hamsters exposed to a HK-

240   95-infected hamster have higher titers of virus in their airways, suggesting that the D614G

241   variant is more highly transmissible than non-D614G SARS-CoV-2 strains (**Figure 5**).

242   Infection with SARS-CoV-2 can range from being asymptomatic to causing severe

243   disease and fatalities; it is not yet well understood which viral factors, together with host factors

244   and conditions, may determine pathogenicity in humans. Besides the insertion of a polybasic

245   cleavage PRRA motif at the S1/S2 junction of the spike protein, which clearly contributes to

246   increased virulence features, and was probably responsible for the initial SARS-CoV-2 cross

247   species transmission event (Andersen et al., 2020; Lau et al., 2020b), other virulence elements

248   are not well defined. The spike D614G variant, which was first recorded in January in China

249   (hCoV-19/Zhejiang/HZ103/2020; 24 January 2020) and shortly thereafter in Germany (hCoV-

250   19/Germany/BavPat1-Chvir929/2020; 28 January 2020), was found to have subsequently

251   become the dominant population in multiple countries, suggesting SARS-CoV-2 is adapting

252   to become more transmissible in humans. Host adaptation of an emerging virus in a naive

253   population is generally believed to involve the virus gaining more efficient replicative ability

254   while gradually decreasing its pathogenicity in the new host. It is not clear if the spike D614G

255   variant will drive SARS-CoV-2 towards this evolutionary pathway. The more pathogenic

256   features of the HK-95 strain, which carries the D614G substitution, observed in hamsters in

257   this study could be due to the high replication efficiency of this strain in animals, given that

258   hamsters are highly susceptible to SARS-CoV-2 infection. This is consistent with our

259   transcriptome analysis of lung tissues from infected hamsters, which revealed no significant

260   difference between host responses to infection with 614D or 614G strains (**Figure 4 and S4**).

261   However, the contact transmission experiment demonstrated that HK-95 exhibits higher

262   transmissibility to naive hamsters than HK-13 (**Figure 5**), despite these strains provoking

263   similar pathogenic effects and transcriptome profiles in infected hamsters (**Figure 1, 2, 4 and**

264   **S4**). If the spike D614G mutation is joined by other adaptative mutations as the virus further

265   circulates in humans, it may be postulated that a variant with the D614G substitution together

266   with a deletion in the polybasic cleavage site at the S1/S2 junction could arise, and if so, it may

267   present as a much less pathogenic version of SARS-CoV-2 in the aftermath of the COVID-19

268   pandemic. Nevertheless, human interventions, such as mass vaccination as soon as vaccines

269   are available, and preexisting immunity from prior infections are likely to drive the evolution

270   of variants that can evade host immunity.

271   The increased transmissibility of the D614G SARS-CoV-2 strain is likely due to its

272   higher replication ability. How the spike D614G mutation enhances virus replication and

273   consequently transmissibility has not been defined. We and others have shown that D614G

274   variant spike proteins are more efficiently cleaved into S1 and S2 subunits in cells (**Figure 5B**)

275   (Daniloski et al., 2020; Zhang et al., 2020b). Two synonymous mutations, *5'UTR*-C241T and

276   *Orf1a*-C3037T, and one nonsynonymous mutation, *Orf1b*-P314L, are consistently linked in

277   D614G variant strains (**Table 1**). It remains to be investigated whether these mutations jointly

278   contribute to the enhanced replication ability of the HK-95 SARS-CoV-2 isolate. Of note,

279   *Orf1b*-P314L lies within the RNA-dependent RNA polymerase (RdRp) region, suggesting this

280   mutation may play a causative role on enhanced viral replication.   Further studies, including

281   structural and functional analyses, will provide necessary information for understanding the

282   molecular basis underlying the D614G-associated SARS-CoV-2 phenotype.

283

284

292 **Author contribution**

293 B.W.M. and H.C. designed the studies; B.W.M., C.J.C., S-Y.L., S.D., P.C., A.J.Z., A.C-Y.L.,

294 H.L., S.L., T.T-L.N., H-Y.L., E.L-K.L., K.S-S.L,.P.W. and K-H.C. performance experiments;

295 B.W.M., C.J.C., S-Y.L., A.J.Z., K.K-W.T., J.F-W.C, K-Y.Y., G.K-H.S., and H.C. analyzed the

296 data; B.W. M., C. J.C., G. K-H. S. and H.C. wrote the paper.

297 **Competing Interests statement**

298 The authors declare no conflict of interests.

299

300

301

302

11

Materials and Methods

Virus

The SARS-CoV-2 isolates HK-8 (MT835139), HK-13 (MT835140), HK-15 (MT835141), HK-92 (MT835142) and HK-95 (MT835143) were isolated from specimens obtained from five laboratory-confirmed COVID-19 patients using Vero E6 cells (ATCC; CRL-15786). All experiments involving SARS-CoV-2 viruses were conducted in a Biosafety Level-3 laboratory. For animal challenge, viral stocks were prepared after two serial passages of isolated virus in Vero E6 cells in Dulbecco's Modified Eagle Medium (DMEM) (Thermo Fisher Scientific) supplemented with 5% fetal bovine serum (Thermo Fisher Scientific), and 100 IU penicillin G/ml and 100 ml streptomycin sulfate/ml (Thermo Fisher Scientific). Virus titers were then determined by plaque assay using Vero E6 cells. Viral RNAs were also obtained from the supernatants of infected cells and then isolated using the QIAamp RNA Viral kit (Qiagen) and subjected to whole viral genome sequencing.

Hamster infection

Female golden Syrian hamsters, aged 8-9 weeks old, were obtained from the Laboratory Animal Unit, the University of Hong Kong (HKU). All experiments were performed in a Biosafety Level-3 animal facility at the LKS Faculty of Medicine, HKU. All animal studies were approved by the Committee on the Use of Live Animals in Teaching and Research, HKU. Virus stocks were diluted with phosphate-buffered saline (PBS) to 2×10^4 PFU/ml. Hamsters were anesthetized with ketamine (150mg/kg) and xylazine (10 mg/mg) and then intranasally inoculated with 50 ul of diluted virus stock containing 10^3 PFU of virus or 50 ul PBS (mock infection control). Body weights were monitored daily for 5 days. Nasal washes were collected from hamsters at 3 and 5 dpi. Total nucleic acid was extracted from 140 ul of sample fluid using the QIAamp RNA Viral kit (Qiagen) and eluted with 30 ul of DEPC-treated water. Seven ul RNA was used for reverse transcription using MultiScribe Reverse Transcriptase (Thermofisher). cDNA was subsequently used for real-time qPCR using TB Green Premix Ex Taq (Tli RNase H Plus) (Takara). Viral RNA from nasal washes was also used for whole viral genome sequencing. Hamsters were euthanized at 5 dpi and lung tissues collected for histopathology, determination of viral load and RNA sequencing.

Viral load determination and histopathology

12

336 Lung right lobes (superior, middle and inferior) were homogenized in 1 ml of PBS. After
337 centrifugation at 12,000 rpm for 10 min, the supernatant was harvested, and viral titers
338 determined by plaque assay using Vero E6 cells. Lung left superior lobes were fixed in 4 %
339 paraformaldehyde and then processed for paraffin embedding. The 4 µm tissue sections were
340 stained with haematoxylin and eosin for histopathological examination. Images were obtained
341 with an Olympus BX53 semi-motorized fluorescence microscope using cellSens imaging
342 software.

343

RNA sequencing of hamster lung tissues

345 Lung left inferior lobes from hamsters were cut into pieces and lysed using the RA1 lysis buffer
346 provided with the NucleoSpin® RNA Plus kit (Macherey-Nagel). RNA extraction was then
347 performed according to the manufacturer's instructions, including an on-column genomic
348 DNA digestion step. 1 µg of high-quality total RNA (RIN>8) was used for cDNA library
349 preparation with a KAPA mRNA HyperPrep Kit. The libraries were then denatured and diluted
350 to optimal concentration, before being sequenced on an Illumina NovaSeq 6000 in a 151bp
351 Paired-End format. RNA-seq data used in this study can be accessed in GEO under the
352 accession number GSE156005.

353

Transmission experiment

355 For each virus strain two hamsters were intranasally inoculated with 10^3 PFU of virus. At
356 twenty-four hours post-infection (1 dpi), each infected donor hamster was transferred to a new
357 cage and co-housed with three naïve hamsters for 1 day. At 4 dpi, recipient hamsters were
358 euthanized, and lung and nasal turbinate tissues collected for determination of viral load.

13

359

Differential expression (DE) analysis

360

361 Sequencing reads were aligned to the merged golden hamster (Mesocricetus_auratus, V1.0,

362 ENSEMBL v100) and the SARS-CoV-2 (NCBI Accession: NC_045512.2) genomes using

363 STAR (Dobin et al., 2013). Read counts were extracted using the "--quantMode GeneCounts"

364 argument with STAR for each sample. Counts were used to perform differential expression

365 (DE) with DESeq2 (Love et al., 2014). DE thresholds required genes to have log2FoldChange

366 ≥ 1 and a p-adjusted value ≤ 0.05 to be considered for downstream characterization of gene

367 expression between conditions. Volcano plots were generated using the EnhancedVolcano R

368 package

369 (www.bioconductor.org/packages/release/bioc/vignettes/EnhancedVolcano/inst/doc/Enhance

370 dVolcano.html). Normalized viral gene counts were extracted from DESeq2 output. Boxplots

371 were generated with ggplot2 R package (Wickham, 2016). All analysis was performed through

372 R 4.0 with custom R script.

373

Principal component analysis

374

375 Log2FoldChange values for hamster DEGs for infections with each of the five isolates,

376 contrasted to samples from uninfected animals, were extracted from the results of DESeq2.

377 PCA analysis was performed on these values using the prcomp function from the stats R

378 package. Scatterplots of PCA outputs were generated using the ggplot2 R package.

379

Evolutionary analysis

380

381 The lack of annotation regarding mechanisms underlying the regulation of many biological

382 networks in hamsters required the determination of a well-annotated close relative from which

383 to infer the biological roles of differentially expressed genes in a species with a better

384 representation of the dynamics of the SARS-CoV-2 host response in humans. Evolutionary

385 analysis was performed in accordance to the protocol set by the author (Hall, 2013), using

386 MEGA X software. Briefly, IL6 gene sequence homologs were acquired through an extensive

387 search of the ENSEMBL (v100) database and their identity verified through nBLAST.

388 Sequences were aligned using MUSCLE, with positions with less than 95% coverage being

389 excluded (Edgar, 2004). The evolutionary history of IL6 was inferred using the Maximum

390 Likelihood method and Tamura 3-parameter model (Tamura, 1992).

14

391

Gene set enrichment analysis (GSEA)

392

393 Comprehensive lists of known mouse-hamster gene orthologues were compiled from the

394 BioMart database (Smedley et al., 2015). Differentially expressed hamster genes which were

395 identified to have a mouse orthologue form were retained from the orthologous gene list. These

396 lists of orthologues were matched to genes categorized into Gene Ontology (GO) biological

397 processes. The top 30 GO terms which were identified to have the most significant enrichment

398 (FDR $\leq$ 0.05) across infected conditions were determined. A comparison between HK-95 and

399 non-D614G isolates was also conducted. Heatmaps of significant GO groups were generated

400 using the ComplexHeatmap R package (Gu et al., 2016).

401

402 **Whole viral genome sequencing:**

403 **Reverse transcription and viral genome amplification using multiplex PCR**

404 Viral RNA extracted from cell cultures and nasal washes was treated using the TURBO DNA-

405 free Kit (ThermoFisher Scientific) to remove residual host DNA, followed by synthesis of

406 single-strand cDNA using SuperScript IV reverse transcriptase (Invitrogen). The viral cDNA

407 was then enriched through multiplex tiling polymerase chain reaction (PCR), as described in

408 the ARTIC network (https://artic.network/ncov-2019) (Supplementary material).

409 **Nanopore sequencing of viral genome**

410 The input viral cDNA amplicons for individual samples were normalized to 5 ng, followed by

411 end-repairing and adapter ligation according to official 1D sequencing protocols (SQK-

412 LSK109, Oxford Nanopore). The libraries were sequenced on a Nanopore MinION device

413 using an R9.4.1 flow cell for 48 hours. Nanopore sequencing data were analyzed using a

414 modified Artic Network nCoV-2019 novel coronavirus bioinformatics protocol (Luo et al.,

415 2020) (Supplementary material).

416 **Illumina MiSeq sequencing of viral genome**

417 A total of 100 ng of multiplex PCR amplicons were subjected to library preparation and dual-

418 indexing using a KAPA HyperPrep Kit and a Unique Dual-Indexed Adapter Kit (Roche

419 Applied Science) in accordance with the manufacturer's instructions. Ligated libraries were

420 then enriched by 6-cycle PCR amplification, followed by purification and size selection using

421 AMPure XP beads (Beckman Coulter). The pooled libraries were sequenced using the MiSeq

422 Reagent Kit V2 Nano on an Illumina MiSeq System. The Illumina MiSeq sequencing reads

423 were then demultiplexed and mapped to the reference genome (accession number:

15

424 NC_0.45512.2) using Samtools v1.7. Variants were called with Freebayes v1.0.0

425 (https://arxiv.org/abs/1207.3907) with the haploid setting, with a minimum base quality and depth

426 of coverage of Q30 and 50x, respectively.

427 **Phylogenetic analysis**

428 To determine the phylogenetic placement of our strains in the global phylogeny of SARS-CoV-

429 2, a total of 100 SARS-CoV-2 genomes were downloaded from the GISAID severe acute

430 respiratory syndrome coronavirus 2 data hub (Elbe and Buckland-Merrett, 2017). A

431 phylogenetic tree was constructed with PhyML (v3.0) using the maximum likelihood algorithm.

432 A best-fit substitution model for phylogenetic analysis was created using the Akaike

433 information criterion, in which the general time reversible model with a fixed proportion of

434 invariable sites (+I) was selected (Guindon et al., 2010). Bootstrap replicates were set at 1000×,

435 and the maximum-likelihood phylogenetic tree was rooted on the earliest published genome of

436 SARS-CoV-2 (accession no.: NC_045512.2).

437

438 **References**

439 Andersen, K.G., Rambaut, A., Lipkin, W.I., Holmes, E.C., and Garry, R.F. (2020). The proximal origin of
440 SARS-CoV-2. Nat Med *26*, 450-452.

441 Becerra-Flores, M., and Cardozo, T. (2020). SARS-CoV-2 viral spike G614 mutation exhibits higher case
442 fatality rate. Int J Clin Pract, e13525.

443 Blanco-Melo, D., Nilsson-Payant, B.E., Liu, W.C., Uhl, S., Hoagland, D., Moller, R., Jordan, T.X., Oishi, K.,
444 Panis, M., Sachs, D.*, et al.* (2020). Imbalanced Host Response to SARS-CoV-2 Drives Development of
445 COVID-19. Cell *181*, 1036-1045 e1039.

446 Chan, J.F., Yuan, S., Kok, K.H., To, K.K., Chu, H., Yang, J., Xing, F., Liu, J., Yip, C.C., Poon, R.W.*, et al.*
447 (2020a). A familial cluster of pneumonia associated with the 2019 novel coronavirus indicating person-
448 to-person transmission: a study of a family cluster. Lancet *395*, 514-523.

449 Chan, J.F., Zhang, A.J., Yuan, S., Poon, V.K., Chan, C.C., Lee, A.C., Chan, W.M., Fan, Z., Tsoi, H.W., Wen,
450 L.*, et al.* (2020b). Simulation of the clinical and pathological manifestations of Coronavirus Disease
451 2019 (COVID-19) in golden Syrian hamster model: implications for disease pathogenesis and
452 transmissibility. Clin Infect Dis.

453 Chen, J., Wang, R., Wang, M., and Wei, G.W. (2020a). Mutations Strengthened SARS-CoV-2 Infectivity.
454 J Mol Biol *S0022-2836*, 30456-30453.

455 Chen, N., Zhou, M., Dong, X., Qu, J., Gong, F., Han, Y., Qiu, Y., Wang, J., Liu, Y., Wei, Y.*, et al.* (2020b).
456 Epidemiological and clinical characteristics of 99 cases of 2019 novel coronavirus pneumonia in Wuhan,
457 China: a descriptive study. Lancet *395*, 507-513.

458 Daniloski, Z., Guo, X., and Sanjana, N.E. (2020). The D614G mutation in SARS-CoV-2 Spike increases
459 transduction of multiple human cell types. bioRxiv.

460 Deng, X., Gu, W., Federman, S., du Plessis, L., Pybus, O.G., Faria, N., Wang, C., Yu, G., Bushnell, B., Pan,
461 C.Y.*, et al.* (2020). Genomic surveillance reveals multiple introductions of SARS-CoV-2 into Northern
462 California. Science *369*, 582-587.

463 Dobin, A., Davis, C.A., Schlesinger, F., Drenkow, J., Zaleski, C., Jha, S., Batut, P., Chaisson, M., and
464 Gingeras, T.R. (2013). STAR: ultrafast universal RNA-seq aligner. Bioinformatics *29*, 15-21.

465 Dong, E., Du, H., and Gardner, L. (2020). An interactive web-based dashboard to track COVID-19 in real
466 time. Lancet Infect Dis *20*, 533-534.

467 Edgar, R.C. (2004). MUSCLE: a multiple sequence alignment method with reduced time and space
468 complexity. BMC Bioinformatics *5*, 113.
469 Elbe, S., and Buckland-Merrett, G. (2017). Data, disease and diplomacy: GISAID's innovative
470 contribution to global health. Glob Chall *1*, 33-46.
471 Fauver, J.R., Petrone, M.E., Hodcroft, E.B., Shioda, K., Ehrlich, H.Y., Watts, A.G., Vogels, C.B.F., Brito,
472 A.F., Alpert, T., Muyombwe, A.*, et al.* (2020). Coast-to-Coast Spread of SARS-CoV-2 during the Early
473 Epidemic in the United States. Cell *181*, 990-996 e995.
474 Forster, P., Forster, L., Renfrew, C., and Forster, M. (2020). Phylogenetic network analysis of SARS-
475 CoV-2 genomes. Proc Natl Acad Sci U S A *117*, 9241-9243.
476 Gong, Y.N., Tsao, K.C., Hsiao, M.J., Huang, C.G., Huang, P.N., Huang, P.W., Lee, K.M., Liu, Y.C., Yang,
477 S.L., Kuo, R.L.*, et al.* (2020). SARS-CoV-2 genomic surveillance in Taiwan revealed novel ORF8-deletion
478 mutant and clade possibly associated with infections in Middle East. Emerg Microbes Infect, 1-37.
479 Gu, Z., Eils, R., and Schlesner, M. (2016). Complex heatmaps reveal patterns and correlations in
480 multidimensional genomic data. Bioinformatics *32*, 2847-2849.
481 Guindon, S., Dufayard, J.F., Lefort, V., Anisimova, M., Hordijk, W., and Gascuel, O. (2010). New
482 algorithms and methods to estimate maximum-likelihood phylogenies: assessing the performance of
483 PhyML 3.0. Syst Biol *59*, 307-321.
484 Hall, B.G. (2013). Building phylogenetic trees from molecular data with MEGA. Mol Biol Evol *30*, 1229-
485 1235.
486 Hoffmann, M., Kleine-Weber, H., and Pohlmann, S. (2020). A Multibasic Cleavage Site in the Spike
487 Protein of SARS-CoV-2 Is Essential for Infection of Human Lung Cells. Mol Cell *78*, 779-784 e775.
488 Jaimes, J.A., Millet, J.K., and Whittaker, G.R. (2020). Proteolytic Cleavage of the SARS-CoV-2 Spike
489 Protein and the Role of the Novel S1/S2 Site. iScience *23*, 101212.
490 Ji, T., Chen, H.L., Xu, J., Wu, L.N., Li, J.J., Chen, K., and Qin, G. (2020). Lockdown contained the spread
491 of 2019 novel coronavirus disease in Huangshi city, China: Early epidemiological findings. Clin Infect
492 Dis.
493 Korber, B., Fischer, W.M., Gnanakaran, S., Yoon, H., Theiler, J., Abfalterer, W., Hengartner, N., Giorgi,
494 E.E., Bhattacharya, T., Foley, B.*, et al.* (2020). Tracking Changes in SARS-CoV-2 Spike: Evidence that
495 D614G Increases Infectivity of the COVID-19 Virus. Cell *182*, 812-827.
496 Lau, H., Khosrawipour, V., Kocbach, P., Mikolajczyk, A., Schubert, J., Bania, J., and Khosrawipour, T.
497 (2020a). The positive impact of lockdown in Wuhan on containing the COVID-19 outbreak in China. J
498 Travel Med *27*.
499 Lau, S.Y., Wang, P., Mok, B.W., Zhang, A.J., Chu, H., Lee, A.C., Deng, S., Chen, P., Chan, K.H., Song, W.*,
500 et al.* (2020b). Attenuated SARS-CoV-2 variants with deletions at the S1/S2 junction. Emerg Microbes
501 Infect *9*, 837-842.
502 Li, Q., Wu, J., Nie, J., Zhang, L., Hao, H., Liu, S., Zhao, C., Zhang, Q., Liu, H., Nie, L.*, et al.* (2020). The
503 Impact of Mutations in SARS-CoV-2 Spike on Viral Infectivity and Antigenicity. Cell *S0092-8674*, 30877-
504 30871.
505 Liu, Y., Ning, Z., Chen, Y., Guo, M., Liu, Y., Gali, N.K., Sun, L., Duan, Y., Cai, J., Westerdahl, D.*, et al.*
506 (2020). Aerodynamic analysis of SARS-CoV-2 in two Wuhan hospitals. Nature *582*, 557-560.
507 Love, M.I., Huber, W., and Anders, S. (2014). Moderated estimation of fold change and dispersion for
508 RNA-seq data with DESeq2. Genome Biol *15*, 550.
509 Luo, R., Wang, C.-L., Yat-Sing, W., Tang, C.-I., Liu, C.-M., Chi-Ming., L., and Lam, T.-W. (2020). Exploring
510 the limit of using a deep neural network on pileup data for germline variant calling. Nature *2*,
511 pages220–227.
512 Mahase, E. (2020). Covid-19: WHO declares pandemic because of "alarming levels" of spread, severity,
513 and inaction. BMJ *368*, m1036.
514 Sanchez-Pacheco, S.J., Kong, S., Pulido-Santacruz, P., Murphy, R.W., and Kubatko, L. (2020). Median-
515 joining network analysis of SARS-CoV-2 genomes is neither phylogenetic nor evolutionary. Proc Natl
516 Acad Sci U S A *117*, 12518-12519.

17

517 Smedley, D., Haider, S., Durinck, S., Pandini, L., Provero, P., Allen, J., Arnaiz, O., Awedh, M.H., Baldock,
518 R., Barbiera, G*., et al.* (2015). The BioMart community portal: an innovative alternative to large,
519 centralized data repositories. Nucleic Acids Res *43*, W589-598.
520 Su, Y.C.F., Anderson, D.E., Young, B.E., Linster, M., Zhu, F., Jayakumar, J., Zhuang, Y., Kalimuddin, S.,
521 Low, J.G.H., Tan, C.W*., et al.* (2020). Discovery and Genomic Characterization of a 382-Nucleotide
522 Deletion in ORF7b and ORF8 during the Early Evolution of SARS-CoV-2. mBio *11*.
523 Tamura, K. (1992). Estimation of the number of nucleotide substitutions when there are strong
524 transition-transversion and G+C-content biases. Mol Biol Evol *9*, 678-687.
525 Wickham, H. (2016). ggplot2: Elegant Graphics for Data Analysis. pringer-Verlag New York.
526 Wong, Y.C., Lau, S.Y., Wang To, K.K., Mok, B.W.Y., Li, X., Wang, P., Deng, S., Woo, K.F., Du, Z., Li, C*., et
527 al.* (2020). Natural transmission of bat-like SARS-CoV-2PRRA variants in COVID-19 patients. Clin Infect
528 Dis.
529 Wu, F., Zhao, S., Yu, B., Chen, Y.M., Wang, W., Song, Z.G., Hu, Y., Tao, Z.W., Tian, J.H., Pei, Y.Y*., et al.*
530 (2020). A new coronavirus associated with human respiratory disease in China. Nature *579*, 265-269.
531 Zhang, A.J., Lee, A.C., Chu, H., Chan, J.F., Fan, Z., Li, C., Liu, F., Chen, Y., Yuan, S., Poon, V.K*., et al.*
532 (2020a). SARS-CoV-2 infects and damages the mature and immature olfactory sensory neurons of
533 hamsters. Clin Infect Dis.
534 Zhang, L., Jackson, C.B., Mou, H., Ojha, A., Rangarajan, E.S., Izard, T., Farzan, M., and Choe, H. (2020b).
535 The D614G mutation in the SARS-CoV-2 spike protein reduces S1 shedding and increases infectivity.
536 bioRxiv.
537 Zhang, X., Tan, Y., Ling, Y., Lu, G., Liu, F., Yi, Z., Jia, X., Wu, M., Shi, B., Xu, S*., et al.* (2020c). Viral and
538 host factors related to the clinical outcome of COVID-19. Nature *583*, 437-440.
539 Zhou, P., Yang, X.L., Wang, X.G., Hu, B., Zhang, L., Zhang, W., Si, H.R., Zhu, Y., Li, B., Huang, C.L*., et al.*
540 (2020a). A pneumonia outbreak associated with a new coronavirus of probable bat origin. Nature *579*,
541 270-273.
542 Zhou, Z., Ren, L., Zhang, L., Zhong, J., Xiao, Y., Jia, Z., Guo, L., Yang, J., Wang, C., Jiang, S*., et al.* (2020b).
543 Heightened Innate Immune Responses in the Respiratory Tract of COVID-19 Patients. Cell Host
544 Microbe *27*, 883-890 e882.

545

Figure legends

Figure 1. **Body weight and histopathological changes in golden Syrian hamsters challenged with different strains of SARS-CoV-2.** (A) Body weight change in hamsters after viral infection. Body weights of virus-infected and mock-infected hamsters (n=3) were monitored daily for 5 days. Data are shown as the mean ± SD percentages of the starting weight. (B) Haemotoxylin and eosin (H&E) staining of lung sections from SARS-CoV-2 (HK-8, HK-13 and HK-95) infected hamsters, collected at 5 days post-infection (dpi). The lower photographs depict higher magnification images of the regions denoted by circles in upper photographs (upper photographs = 500x magnification). **HK-8**: Upper panel shows patchy inflammatory damage with areas showing peribronchiolar and perivascular infiltration, blood vessel congestion and areas of alveolar wall thickening, while alveolar exudation and infiltration were not apparent. Lower panel: (1) bronchiolar luminal exudation with cell debris (arrows), surrounding alveolar wall infiltration (arrowhead); (2) a small sized blood vessel shows perivascular and endothelial infiltration (arrows), but the surrounding alveolar space shows no infiltration or exudation (arrowhead); (3) alveolar wall capillary congestion and moderate infiltration (arrow). **HK-13**: Upper panel shows diffuse lung tissue inflammatory damage with massive alveolar space infiltration and exudation; perivascular infiltration and endothelial infiltration can be observed in all blood vessels in this lung section. Lower panel: (1) mild bronchiolar luminal exudation with cell debris (arrows); (2) a large blood vessel shows severe endothelial infiltration and vessel wall infiltration (arrows) and surrounding alveolar space infiltration and exudation (arrowheads); (3) alveolar structure destroyed by septal edema and alveolar space infiltration and fluid exudation (arrows). **HK-95**: Upper panel shows diffuse lung tissue damage with massive alveolar space exudation and infiltration; all blood vessels in the field show perivascular infiltration and endothelial infiltration. A moderate degree of bronchiolar epithelial cell death and luminal exudation is seen. Lower panel: (1) bronchiolar luminal exudation with cell debris (arrow); (2) a medium sized blood vessel shows severe endothelial infiltration and vessel wall infiltration (arrows), with alveolar space infiltration in alveoli surrounding the vessel (arrowheads); (3) alveolar structure has reduced cellularity but shows alveolar septal edema and alveolar space fluid exudation (arrows).

Figure 2. Viral replication and transcriptome response to different SARS-CoV-2 isolates in hamster lungs. (A) Virus replication in hamsters infected with different SARS-CoV-2 isolates. Three to seven hamsters per group were euthanized on day 5 post-infection for viral titration. Virus titers in lungs were determined by plaque assays (PFU/ml) and displayed as

19

580   mean (± SEM). (B) Average viral gene expression in samples from hamsters infected with each

581   isolate. Horizontal black lines indicate the overall mean of average expression values for viral

582   genes per isolate. (C) Transcriptome response to different SARS-CoV-2 isolates in hamster

583   lungs. Principal component analysis of global transcription profiles of significantly expressed

584   host genes for infections with each isolate, compared to uninfected conditions. Individual data

585   points and means ± SEM are also shown. Statistical significance was calculated by Mann

586   Whitney Wilcoxon Test; * denotes *p<0.05*, ** denotes *p<0.005* and ns denotes *non-significant*.

587

588   **Figure 3**. **Volcano plots comparing differentially expressed genes (DEGs) in HK-8-**

589   **infected hamster lungs to those in hamsters infected with HK-13, HK-15, HK-92 or HK-**

590   **95**. DEGs: log2FoldChange $\geqslant$ 1 and p-adjusted value $\leqslant$ 0.05.

591

592   **Figure 4. Differential gene expression in SARS-CoV-2 infection.**

593   Heatmap depicting the expression levels of enriched gene sets in lungs collected from hamsters

594   infected with the indicated viruses at 5 dpi. Gene enrichment was performed on differentially

595   expressed genes identified in comparisons between infections with each of the 5 different

596   SARS-CoV-2 isolates and uninfected controls. DEGs that were identified as hamster–mouse

597   orthologues were extracted and matched to gene members of mouse GO biological processes.

598   The top 30 GO biological processes with significant enrichment (FDR $\leqslant$ 0.05) across infected

599   conditions are displayed.

600

601   **Figure 5. D614G enhances efficiency of spike protein cleavage and transmission of SARS-**

602   **CoV-2 isolates in hamsters.**

603   (A) Transmission of SARS-CoV-2 isolates. For each isolate, two groups of three naïve

604   hamsters were each co-housed with one inoculated donor on day 1 post-infection. Viral loads

605   (PFU/ml) in lungs and nasal turbinates of naïve contact hamsters (n=6 per isolate) at 3 days

606   after exposure are shown. Data are presented as individual data points and means ± SEM.

607   Statistical significance was calculated by Mann Whitney Wilcoxon Test; (*) p value < 0.05, ns

608   – not significant. (B) The human codon-optimized spike gene of Wuhan-Hu-1 SARS-CoV-2

609   was cloned into the Flag-tagged-pCAGEN vector. A pCAGEN-S-D614G-Flag mutant was

610   constructed using a QuikChange site-directed mutagenesis kit (Agilent) according to the

611   standard protocol. Protein expression and cleavage in transfected HEK293T-ACE2 cells was

20

612   demonstrated with western blotting. Rabbit anti-Spike RBD was used to detect the spike and

613   S1 proteins, and mouse anti–Flag M2 to detect S2 protein (Supplementary materials).
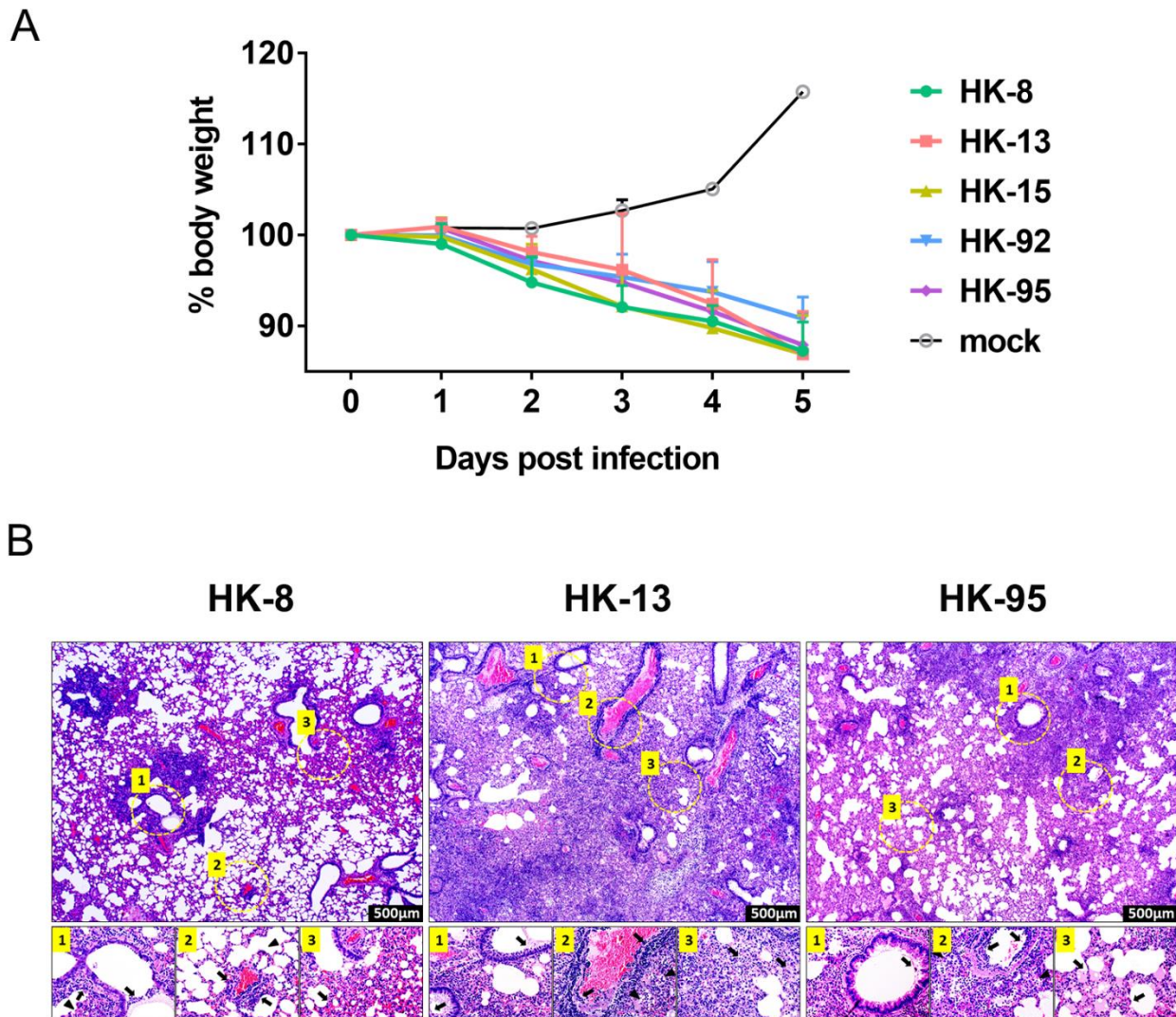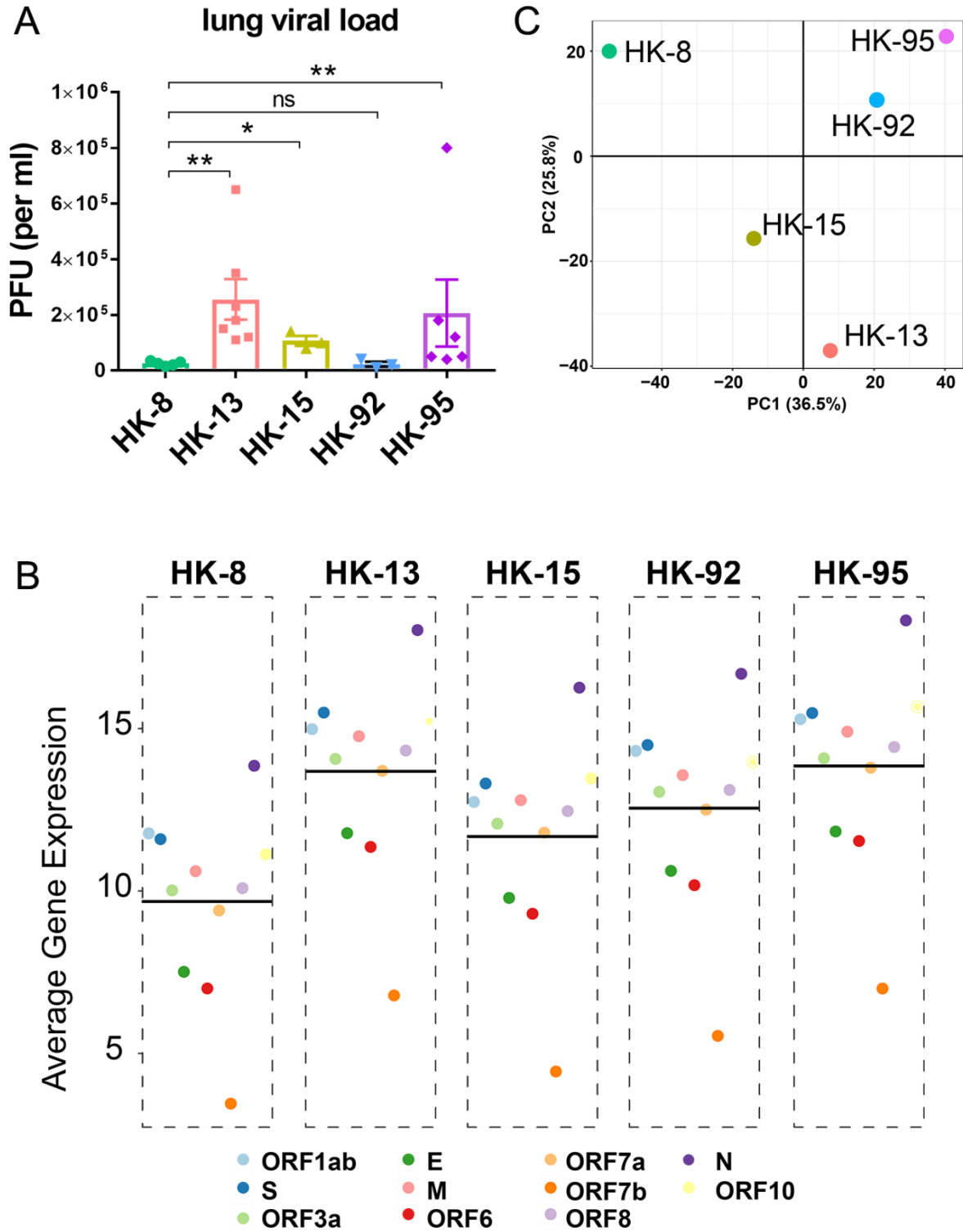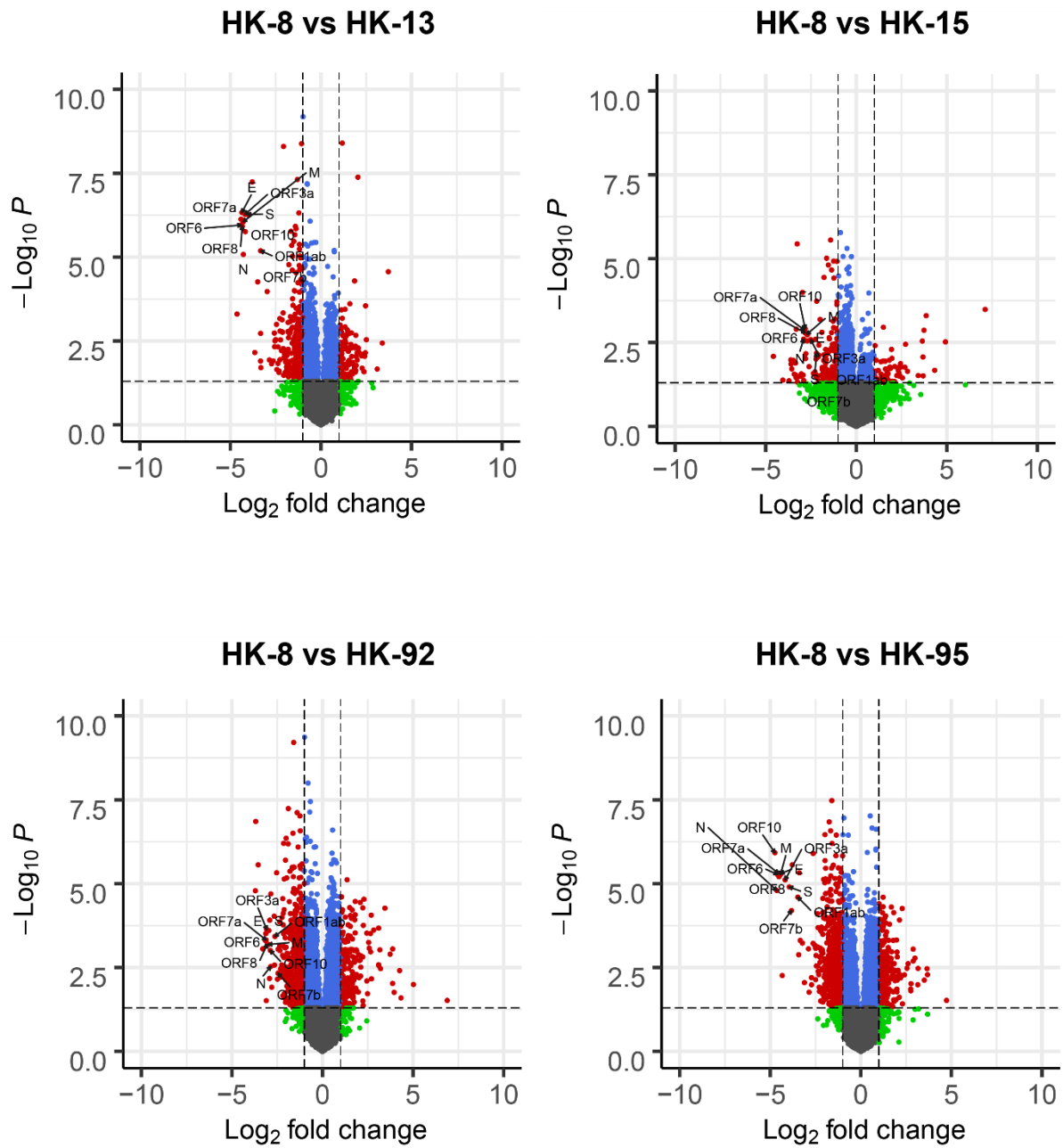
614

615

616

617

Figure 1

A

B

Figure 2

Figure 3

Figure 4

Figure 5
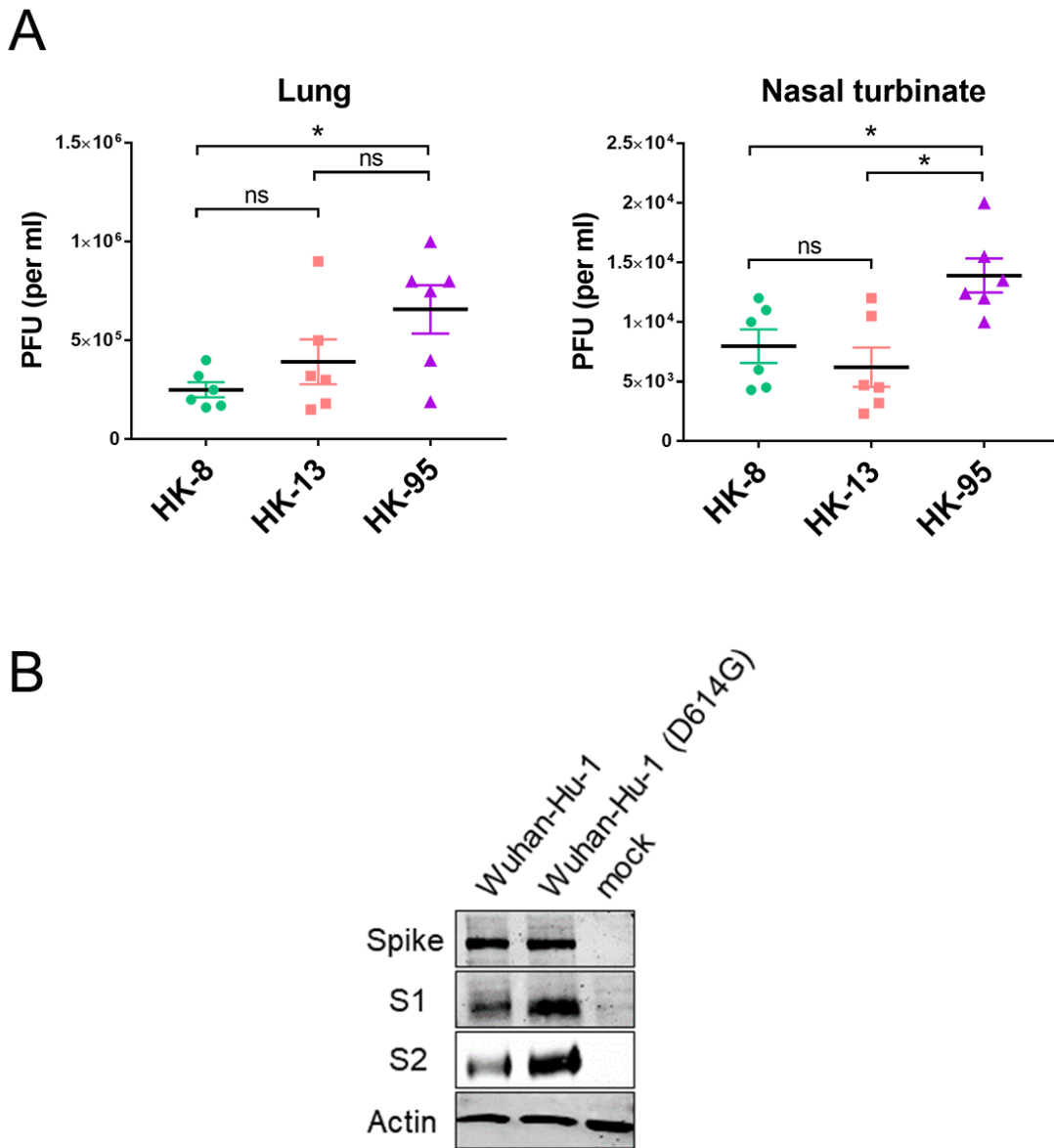
Table 1.   Sequence diversity in SARS-CoV-2 isolates

SITE	Wuhan-Hu-1	8	13	15	92	95	AA	ORF	Occurrence frequency $
241	C	-	-	-	-	T	--	UTR	>50
1515	A	-	-	-	G	-	H417R	Orf1a	17
3037	C	-	-	-	-	T	--	Orf1a	>50
4093	C	-	-	-	C/T*	-	--	Orf1a	1
4899	A	-	-	-	A/G*	-	H1545R	Orf1a	0
5310	C	C/T*	-	-	-	-	T1682I	Orf1a	12
8092	C	T	-	-	-	-	--	Orf1a	7
9223	C	-	-	-	T	-	--	Orf1a	20
10981	G	-	-	G/T#	-	-	--	Orf1a	0
11083	G	T	-	-	T	-	L3606F	Orf1a	>50
12565	G	-	-	-	T	-	Q4100H	Orf1a	0
14408	C	-	-	-	-	T	P314L	Orf1b	>50
14805	C	-	-	-	T	-	--	Orf1b	>50
17247	T	-	-	-	C	-	--	Orf1b	>50
17423	A	-	G	G	-	-	Y1319C	Orf1b	>50
20667	A	-	G	-	-	-	--	Orf1b	1
21137	A	A/G**	-	-	-	-	K2557R	Orf1b	33
23403	A	-	-	-	-	G	D614G	S	>50
26144	G	-	-	-	T	-	G251V	Orf3a	>50
27920	C	-	C/T#	-	-	-	--	Orf8	1
28854	C	-	T	T	-	-	S194L	N	>50

* Reported variants with variant frequency between 10% - 30%.

** Reported variants with variant frequency 10% or below

Variant frequency varies between samples derived from the same isolate

$ Data were retrieved on August 6, 2020 from GenBank